Comparison of Fuga and RANS in complex terrain

van der Laan, Paul; Ott, Søren; Meyer Forsting, Alexander; Verelst, David Robert

Publication date:
2018

Document Version
Publisher's PDF, also known as Version of record

Comparison of Fuga and RANS in complex terrain

DTU Wind Energy
E-report

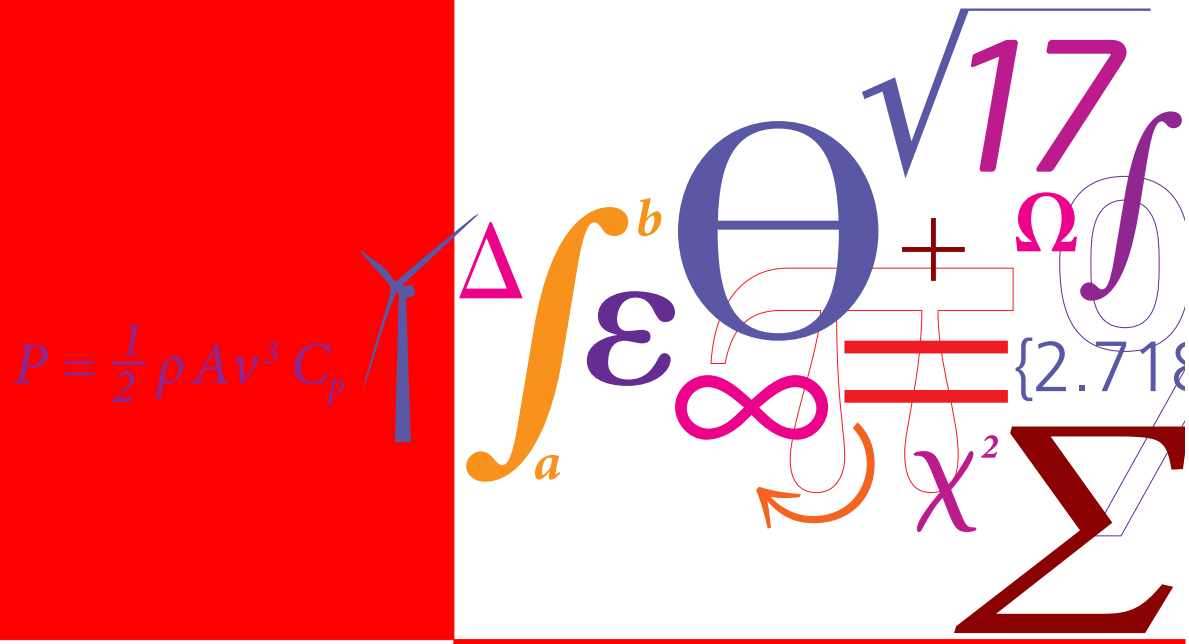

M. Paul van der Laan
Søren Ott
Alexander R. Meyer Forsting
David R. Verelst
DTU Wind Energy E-0173
September 2018

DTU Wind Energy
Department of Wind Energy

Contents

1 Introduction

Modeling wind turbine wakes and wind resources in complex terrain is challenging. High fidelity Computational Fluid Dynamics (CFD) methods can produce accurate results of long term averaged speed up factors for flow over complex terrain although user uncertainty can create large differences between CFD model results [1]. Engineering wake models are often not suited to model wakes in complex terrain because they are developed for wind farms in flat terrain [2]. Fuga [3] is a fast linearized CFD model developed to model wake effects in wind farms for flat terrain and uniform roughness lengths. The base flow in Fuga is an atmospheric surface layer following Monin-Obukhov Similarity Theory [4] and the effect of a wind turbine wake is added as a linear perturbation. Recent work has been carried out to develop a linearized terrain flow model in Fuga. The linearity of this terrain flow model implies that the model can only predict first order perturbations of the terrain and cannot predict flow separation and recirculation zones. In unpublished work, a comparison between the terrain flow model of Fuga and a Reynols-averaged Navier-Stokes (RANS) model as implemented in EllipSys3D [5, 6] has been made for the flow over an axisymmetric Gaussian hill with a moderate maximum slope angle of 17°using eight test cases. This moderate slope angle was chosen to avoid flow separation. The comparison showed that the streamlines of Fuga and EllipSys3D compare well for all eight test cases. Results of this study are presented in Section 3.1 and the comparison is extended with results of speed up factor contours and profiles. In this report, we would like to continue the comparison between the terrain flow model of Fuga and RANS (without wind turbine wakes) for additional test cases that are designed to answer the following three research questions:

1. How well do the wind turbine wake streamlines follow the terrain streamlines?
2. For which slope angles does the terrain flow model of Fuga start to deviate significantly from RANS in terms of streamlines and speed up factors for an axisymmetric Gaussian hill?
3. How well does the terrain flow model of Fuga compare with RANS for a real complex terrain site in terms of speed up factors and velocity profiles?

The methodology and test cases are presented in Section 2. The results are discussed in Section 3.

2 Methodology

2.1 Test cases

Fiveteen test cases are used to compare the terrain flow model of Fuga with RANS from EllipSys3D. Twelve test cases are based on axissymmetric Gaussian hill and are discussed in Section 2.1.1. Three test cases are based on a real complex terrain site and are presented in Section 2.1.2.

2.1.1 Axisymmetric Gaussian hill

The axisymmetric Gaussian hill is defined by the function $g(r)$:

$$g(r) = H \exp\left(-\frac{r^2}{2\sigma^2}\right), \tag{1}$$

where H is the height of the hill, r is the horizontal radial distance from the hill top ($r^2 = x^2 + y^2$) and σ is the radial standard deviation. The maximum slope of the hill $|dg/dr|$ is located at $r = \pm\sigma$ and is equal to:

$$\left|\frac{dg}{dr}\right| = \frac{H}{\sigma} \exp\left(-\frac{1}{2}\right) \tag{2}$$

Taking the arctangent of the right hand side of eq. (2) gives the angle of maximum slope α:

$$\alpha = \arctan\left(\xi \exp\left(-\frac{1}{2}\right)\right), \tag{3}$$

where $\xi = \frac{H}{\sigma}$. Likewise, the standard deviation can be calculated from a given maximum slope angle:

$$\sigma = \frac{H \exp\left(-\frac{1}{2}\right)}{\tan \alpha}, \tag{4}$$

The first eight test cases are based on previous unpublished work, where an axisymmetric Gaussian hill with a moderate slope angle of 17°and a hill height of 126 m are used. The RANS simulations are carried out without and with a simplified onshore version of the NREL-5MW wind turbine where the hub height is set equal to the rotor diameter, a constant thrust coefficient is set to 8/9, a uniform thrust force distribution is employed and tangetial forces are neglected. In the first four test cases the rotor diameter is the same as the hill height (126 m). The location of the wind turbine is varied between the first four test cases: $\{x,y\} = \{0,0\}$ (at the hill top), $\{x,y\} = \{-5D,0\}$ (in front of the hill top), $\{x,y\} = \{0,\sigma\}$ (at the side of the hill where the largest gradient is present) and $\{x,y\} = \{-5D,\sigma\}$. The same variation of wind turbine locations are used in Test cases 5-8 but the rotor diameter is set $H/3 = 42$ m. The last four test cases (Cases 9-12) are added in the present work where the hill angle α is increased from 20 to 40°. In these test cases, a wind turbine is placed at the hill top with a rotor diameter $H/3$. Atmospheric stability can have a large impact on the flow over complex terrain. In the present work, we only consider neutral atmospheric stability for simplicity and the inflow profile of all test cases is based on a logarithmic (neutral) surface layer:

$$U = \frac{u_*}{\kappa} \ln\left(\frac{z' + z_0}{z_0}\right) \tag{5}$$

where z' is the height above the terrain, u_* is the friction velocity set to 0.4 m/s, $\kappa = 0.4$ is the Von Kármán constant and z_0 is the roughness length set to 0.03 m. The choice of u_* does not influence the simulations (without wind turbines) because of the speed up factor is independent of the Reynolds number. The chosen roughness length of 0.03 m is low for complex terrain but sufficient to perform a model comparison. Larger roughness lengths should be investigated in future work.

Table 1: Test cases based on axisymmetric Gaussian hill.

Case	α [°]	D [m]	x_{AD}	y_{AD}
1	17	H	0	0
2	17	H	$-5H$	0
3	17	H	0	σ
4	17	H	$-5H$	σ
5	17	$H/3$	0	0
6	17	$H/3$	$-5H$	0
7	17	$H/3$	0	σ
8	17	$H/3$	$-5H$	σ
9	20	$H/3$	0	0
10	25	$H/3$	0	0
11	30	$H/3$	0	0
12	40	$H/3$	0	0

2.1.2 Shaanxi complex terrain site

Sessarego et al. [7] have investigated an onshore wind farm located in complex terrain site in the Shaanxi province of Northern China. The wind farm consists of twenty-five 2 MW wind turbines that have a 93 m rotor diameter and a 67 m hub height. The Shaanxi complex terrain site and wind farm layout is depicted in the top plots of Figure 1. The horizontal coordinates represent UTM coordinates (zone 49) minus the location of wind turbine (WT) 10. The terrain map is taken from Shuttle Radar Topography Mission (SRTM) data [8]. The contour terrain map is transformed to a gridded file with horizontal and vertical resolution of 40 and 2 m, respectively. Outside a radius of 8 km ($r_{\min} = 8$) around WT 10, the terrain height $h(x,y)$ is

smoothed with a Gaussian filter towards a constant height h_{out} using a standard deviation σ_h of 4 km:

$$h(x,y)_{\text{smoothed}} = [h(x,y) - h_{\text{out}}] \exp\left(-\frac{(r - r_{\min})^2}{2\sigma_h^2}\right) + h_{\text{out}} \tag{6}$$

The constant height of the outer domain h_{out} is calculated as the mean height of the circle at which the Gaussian filtering is first applied (at $r_{\min} = 8$ km and $h_{\text{out}} = 1444.7$ m).

The resulting terrain is depicted in the right plots of Figure 1. The smoothing produce will most likely have an effect of the wind resources at the wind farm location because large terrain features are removed upstream. However, in the present work we do not aim to predict the wind resources accurately but our goal is to compare flow models with each other for a complex terrain site. In addition, it is easier to solve the RANS equations for a terrain site that has a uniform terrain far away from the area of interest.

Three complex terrain test cases (Cases 13-15) are defined where the terrain height (minus the minimum height) is scaled by a factor: 0.1, 0.5 and 1, as listed in Table 2. The maximum terrain height above the minimum height and the maximum slope angle are also shown in Table 2. The local maximum slope angle for each point on the terrain map is calculated by the calculating the slope angle with the eight neighboring grid points ($\arctan(\Delta z/\Delta r)$, where Δz and Δr are the height and horizontal distance between two neighboring grid points) and taking the maximum of the eight slope angles. Since the horizontal grid spacing of the terrain map is 20 m, Δr varies from 20 m to $20\sqrt{2} \approx 28$ m. For a scaling of 1, the maximum slope angle over the entire map is 44°. All test cases are run for single wind direction of 180° and we use a roughness height and friction velocity similar to the axisymmetric Gaussian hill test cases ($z_0 = 0.03$ m and $u_* = 0.4$ m/s).

The relative terrain height and the local maximum slope angles are also depicted in Figure 2 for each scaling factor. The bottom right plot of Figure 2 shows that the highest slope angles are located South and East of the wind farm. We expect that for these wind directions, the inflow of the wind turbines is heavily disturbed by the upstream terrain.

Table 2: Test cases based on Shaanxi complex terrain site.

Case	Scale factor	Maximum height difference [m]	Maximum slope angle [°]
13	0.1	52.2	5.7
14	0.5	261	26
15	1.0	522	45

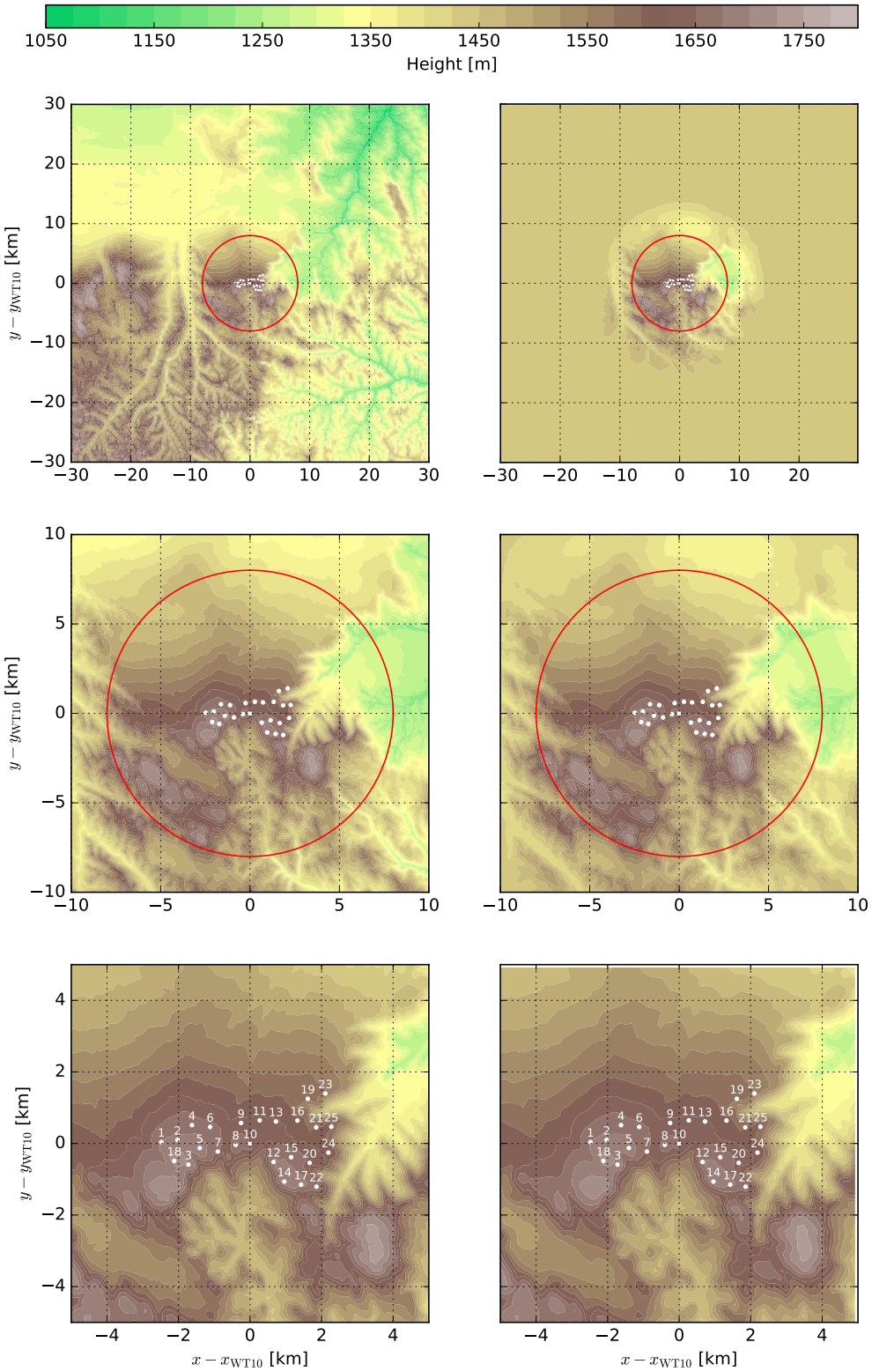

Figure 1: Shaanxi terrain height taken from SRTM data (UTM zone 49). Left column: raw SRTM data. Right column: Gaussian smoothed terrain outside the red circle. Wind turbines are shown as white dots. Reference coordinates: $\{x_{\mathrm{WT10}}, x_{\mathrm{WT10}}\} = \{316864, 4153557\}$ m.

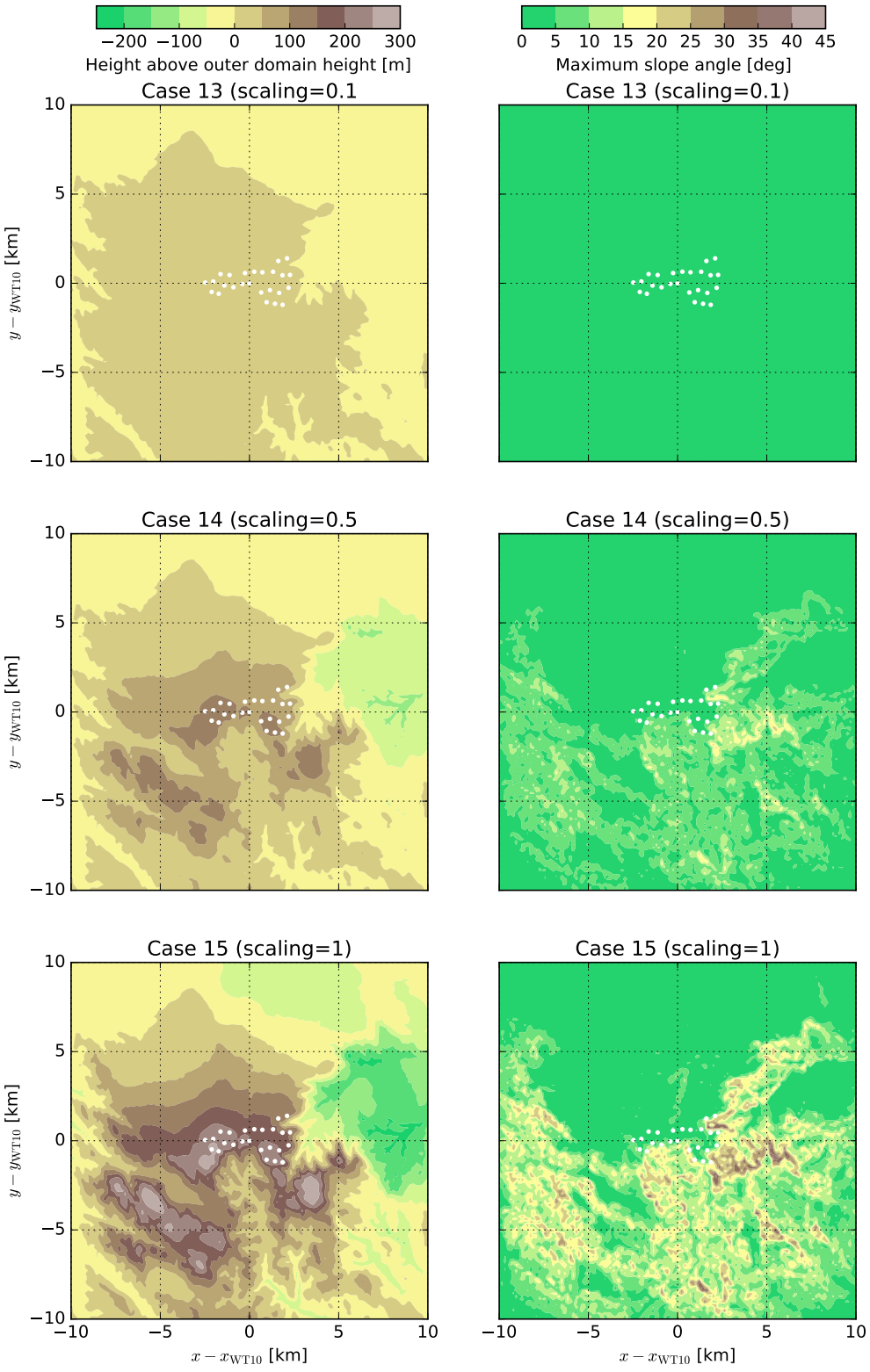

Figure 2: Shaanxi cases. Left column: Terrain height above minimum terrain. Right column: Maximum slope angle in a grid point. Reference coordinates: $\{x_{\mathrm{WT10}}, x_{\mathrm{WT10}}\} = \{316864, 4153557\}$ m, UTM zone 49.

2.2 EllipSys3D

EllipSys3D is a general purpose in-house flow solver of DTU Wind Energy, developed by [5, 6]. In this work, we use a RANS methodology together with the k-ε-f_P turbulence model [9], developed for wind turbine wake simulations over flat terrain. The k-ε-f_P model limits the eddy-viscosity (turbulence mixing) in regions where the velocity gradients are higher than then undisturbed shear, which typically delay the wake recovery compared to standard k-ε model. It should be noted that the eddy-viscosity limiter of the k-ε-f_P model also limits the mixing of the wake of hills. In an unpublished work, the k-ε-f_P model was employed for the Askervein hill test case [10] and the results in terms of speed up factor and turbulence intensity were found to be similar as the standard k-ε model. The k-ε-f_P has recently been employed for wind turbine wakes in more complex terrain without numerical problems [7]. In Section 3.3, results of k-ε-f_P are also compared with the standard k-ε model for the Shaanxi test cases.

2.2.1 Axisymmetric Gaussian hill

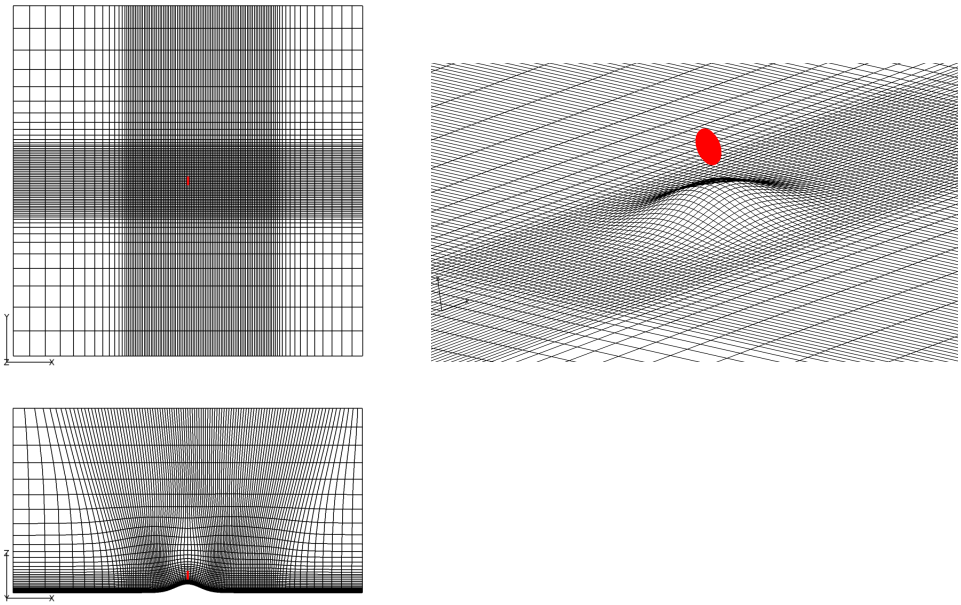

Figure 3: Grid of Axisymmetric Gaussian hill (Cases 1-4), where one in every two grid lines is shown. Red rectangle represents the AD of Case 1. Left, top: Top view of surface grid; left, bottom: Side view $y = 0$; right: 3D view or surface grid around refined wake region.

Test cases 1-12 are based on a Axisymmetric Gaussian hill. In each case, two RANS simulations are carried out: one without a wind turbine and one with a wind turbine that is modeled as an actuator disk (AD) [11] with a constant uniform loading, as discussed in Section 2.1.1. The numerical grid of Cases 1-4 is depicted in Figure 3, where 1 in every 2 grid lines is shown. The grid has the dimensions $40 \times 40 \times 20H^3$ in x, y and z directions, respectively. The x,y origin is defined at the hill top. A refined region is used for $-7 < x/H < 10, -4 < y/H < 4$ to model the wind turbine wake for all possible four AD locations as defined in Table 1. The horizontal spacing in the refined wake region is set to $D/10$ (based on a previously performed grid refinement study [9]), hence a finer grid spacing is used for the Cases 5-8 where the wind turbine is three times smaller with respect to Cases 1-4. The first cell height is set equal to the roughness height of 0.03 m and the cell height increases while moving away from the wall. Most of the cells are located near the surface and the vertical spacing is fine enough to cover at least ten cells over the rotor diameter where the wind turbine wake is resolved. The total amount of cells for Cases 1-4 and Cases 5-12 is 2.8 and 16 million, respectively. An inlet boundary is used at $x = -20H$ and $z = 20H$, at which the logarithmic inflow profile is specified. An outlet boundary is employed at $x = 20H$, at which a zero gradient in the streamwise direction is set. The lateral boundaries ($y = \pm 20H$) are symmetry boundary conditions.

The wall at $z = z_0$ is a rough wall boundary [12]. The numerical domain for the higher slope angle (Cases 9-12) not shown here, but they follow the same methodology as the other cases based on the axisymmetric Gaussian hill.

2.2.2 Shaanxi complex terrain site

The numerical grid of Case 15 is depicted in Figure 4, where 1 in every 2 grid lines is shown. The domain has the dimensions $100 \times 100 \times 11$ km^3 in x, y and z directions, respectively. The origin is located at WT 10 and around this wind turbine, a horizontally refined region of 10×10 km^2 is used with a spacing of 40 m. A grid study of the horizontal spacing is presented in Appendix A. The first cell height is set to 0.03 m and the cells grow while moving away from the wall. 75% of the cells are used within the first 1 km of the domain height (72 cells). The grid consist of 9.8 million cells. Wind turbines are not simulated, but the velocities are extracted at their locations to compare with the terrain model of Fuga. The inlet and outlet boundaries are located at $y = -100km$ and $y = 100km$, respectively. Periodic boundary conditions are used at $x = \pm 100km$. The top boundary condition is also an inlet and the terrain surface is specified as a rough wall boundary condition. The grids of the two other cases based on the Shaanxi site (Cases 13 and 14) follow a similar methodology as Case 15.

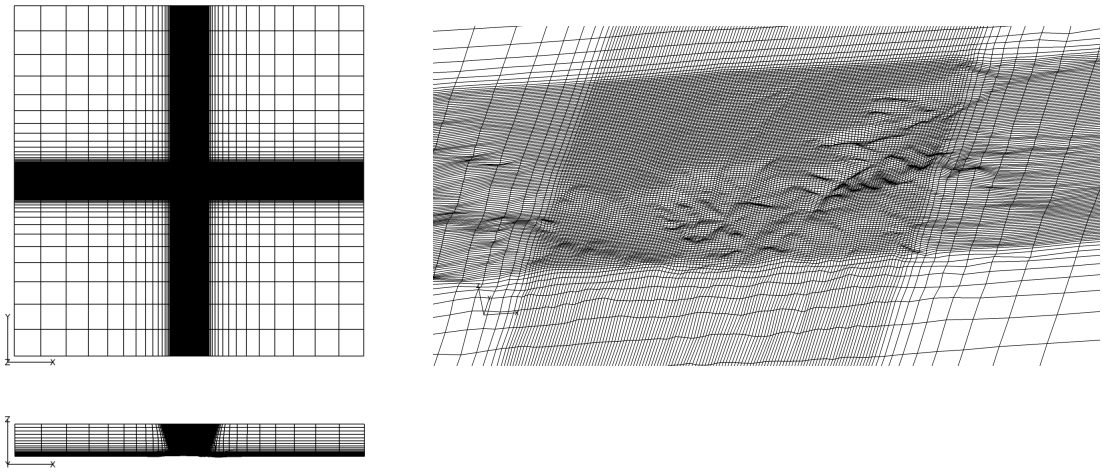

Figure 4: Grid of Shaanxi for a scaling of 1 (Case 15), where one in every two grid lines is shown. Left, top: Top view of surface grid; left, bottom: Side view $y = 0$; right: 3D view or surface grid around refined region of 10×10 km^2.

2.3 Fuga terrain model

The Fuga terrain flow model is a linearized RANS model with a closure based on the eddy viscosity concept. The flow is 'lid driven' with a specified, uniform and horizontal velocity at a certain height, high above the terrain. In the following we assume that this velocity points along the x–axis. The air is taken to be incompressible, and Coriolis forcing and mean pressure gradient are both zero.

For moderately complex terrain, where the mean flow is attached, flow following coordinates $(\acute{x}, \acute{y}, \acute{z})$ can be defined. In this context 'flow following' means that the ground $z = h(x, y)$ is mapped to the surface $\acute{z} = 0$ and that $\acute{y}$ and $\acute{z}$ are constant along streamlines. If one set of flow following coordinates exists there will in fact be infinitely many. We could for example replace $\acute{y}$ by any monotone function of $\acute{y}$ (and likewise for $\acute{z}$) or redefined $\acute{x}$ in any way we wish and still have flow following coordinates. This freedom can be used to demand that the coordinate mapping has certain properties. More specifically, we shall demands that the problem looks as much as possible as flow in uniform, flat terrain.

It turns out to be a good idea to demand that the map is volume preserving. In that case a fluid particle trajectory $x(t)$, i.e.

$$\frac{\mathrm{d}x(t)}{\mathrm{d}t} = u(x(t)), \tag{7}$$

is mapped to a corresponding trajectory $\acute{x}(t)$ that obeys

$$\frac{\mathrm{d}\acute{x}(t)}{\mathrm{d}t} = \acute{u}(\acute{x}(t)) \tag{8}$$

where

$$\acute{u}_i = \frac{\partial \acute{x}_i}{\partial x_j} u_j \tag{9}$$

In other words, $\acute{x}(t)$ is also a streamline, not for u, but for the transformed velocity field $\acute{u}$. Furthermore, for a volume preserving map it can be shown that

$$\frac{\partial \acute{u}_i}{\partial \acute{x}_i} = 0 \tag{10}$$

This looks exactly like the continuity equation for an incompressible fluid, except that $\acute{u}$ is not really a velocity field and the coordinate system is not really Cartesian.

The boundary is rough which means that the u vanishes a distance z_0 away from the surface. In the transformed world we can demand that u, and hence $\acute{u}$, vanishes for $\acute{z} = z_0$. This eliminates the terrain from the boundary conditions, which now look like the boundary conditions in homogeneous, flat terrain.

At the upper boundary, the 'lid', the velocity is uniform and horizontal, hence the original coordinates tend to be flow following near the lid. It is therefore natural to demand that the Jacobian matrix is equal to the unity matrix on the lid, so that the upper boundary conditions become identical in form to those for uniform terrain, viz.

$$\acute{u}(\acute{x}, \acute{y}, \acute{z_{\mathrm{lid}}}) = (u_{\mathrm{lid}}, 0, 0) \tag{11}$$

We now turn to the RANS equation

$$u_j \frac{\partial u_i}{\partial x_j} = \frac{\partial}{\partial x_j} K \left\{ \frac{\partial u_i}{\partial x_j} + \frac{\partial u_j}{\partial x_i} \right\} - \frac{\partial p}{\partial x_i} \tag{12}$$

where p is the pressure normalized by a constant density ρ and K is the eddy viscosity. We should change to new variables, which means making the following substitutions

$$\frac{\partial u_i}{\partial x_j} = \mathrm{J}_{ij} \frac{\partial}{\partial \acute{x}_i} \tag{13}$$

$$u_i = \acute{\mathrm{J}}_{ij} \acute{u}_j \tag{14}$$

where

$$\mathrm{J}_{ij} = \frac{\partial \acute{x}_i}{\partial x_j} \quad \text{and} \quad \acute{\mathrm{J}}_{ij} = \frac{\partial x_i}{\partial \acute{x}_j} \tag{15}$$

J is expressed here in terms of derivatives with respect to x, but it should be expressed in terms of derivatives with respect to the new independent variables $\acute{x}$. This is done by inverting $\acute{\mathrm{J}}$, which amounts to the same as making the co–matrix (since the determinant is equal to 1), e.g.

$$\mathrm{J}_{12} = -\acute{\mathrm{J}}_{21} \acute{\mathrm{J}}_{33} + \acute{\mathrm{J}}_{31} \acute{\mathrm{J}}_{23} \tag{16}$$

It is practical to define a displacement vector λ so that

$$x_i = \acute{x}_i + \lambda_i \tag{17}$$

and

$$\acute{\mathrm{J}}_{ij} = \frac{\partial (\acute{x}_i + \lambda_i)}{\partial \acute{x}_j} = \delta_{ij} + \frac{\partial \lambda_i}{\partial \acute{x}_j} \tag{18}$$

so that

$$u_i = \acute{u}_i + \frac{\partial \lambda_i}{\partial \acute{x}_j}\acute{u}_j \tag{19}$$

Inserting all this into the RANS equation we end up with something like this

$$\acute{u}_j \frac{\partial \acute{u}_i}{\partial \acute{x}_j} = \frac{\partial}{\partial \acute{x}_j} K \left\{ \frac{\partial \acute{u}_i}{\partial \acute{x}_j} + \frac{\partial \acute{u}_j}{\partial \acute{x}_i} \right\} - \frac{\partial p}{\partial \acute{x}_i} + \text{ other terms} \tag{20}$$

The terrain is now completely eliminated if the 'other terms' are in the form of a gradient, which can then be absorbed into the pressure gradient, viz.

$$-\frac{\partial p}{\partial \acute{x}_i} + \text{ other terms} = \frac{\partial \acute{p}}{\partial \acute{x}_i} \tag{21}$$

This is possible if the rotor of the 'other terms' vanishes. Demanding that it does, we end up with equations and boundary conditions of the same form as for flow in homogeneous, flat terrain. All variables, dependent as well as independent, have been redefined: the velocity is not the real velocity, the pressure is not the real pressure and the coordinate system is not Cartesian, but the mathematically the two problems appear the same. The only way that the terrain could show up is through the eddy viscosity K. Normally there are additional variables and equations that determine K, which we have not discussed. If we were dealing with the real, physical variables, then any closure scheme should give $K = \kappa u_* z$ appropriate for flat terrain, and it is tempting to assume that this is the case even in the transformed world because nothing in the mathematical problem suggests otherwise. In other words, we make the assumption that

$$K = \kappa u_* \acute{z} = \kappa u_* (z - \lambda_3) \tag{22}$$

The implication is that

$$(\acute{u}, \acute{v}, \acute{w}) = (\frac{u_*}{\kappa} \log \frac{\acute{z}}{z_0}, 0, 0) \tag{23}$$

$$\acute{p} = 0 \tag{24}$$

Finding $\acute{u}$ is therefore not the problem. After inserting $\acute{u}$ into the Navier stokes equation we get three equations for the four variables λ and p. The fourth equation expresses volume preservation (the Jacobian determinant equals 1). For practical reasons yet another set of coordinates $(\hat{x}, \hat{y}, \hat{z}) = (x, y, \acute{z})$ are used for solving the equations.

The equations are linearized by treating the terrain slope as a small perturbation. The resulting equations are then Fourier transformed in the horizontal dimensions $\hat{x}$ and $\hat{y}$, whereby the problem separates into independent sets of four ordinary differential equations, one set for each horizontal wave vector. These are solved by a dedicated numerical method as described in [3]. Solutions scale with the corresponding Fourier component of the terrain height function h, but are otherwise independent of h. They can therefore be stored as look–up tables that later on can be scaled to fit any given terrain.

Once λ has been found, u can be determined as

$$u = \frac{1 - \hat{\lambda}_{22}}{1 + \hat{\lambda}_{33}}\acute{u} \tag{25}$$

$$v = \frac{\hat{\lambda}_{21}}{1 + \hat{\lambda}_{33}}\acute{u} \tag{26}$$

$$w = \frac{\hat{\lambda}_{31} - \hat{\lambda}_{22}\hat{\lambda}_{31} + \hat{\lambda}_{21}\hat{\lambda}_{32}}{1 + \hat{\lambda}_{33}}\acute{u} \tag{27}$$

where

$$\hat{\lambda}_{ij} = \frac{\partial \lambda_i}{\partial \hat{x}_j} \tag{28}$$

The relation (25) are exact without any linearization. Things clearly go wrong when the denominator $1+\hat{\lambda}_{33}$ vanishes. The same denominator appears in the exact expression for the Jacobian determinant. If h is increased by some global factor, then $\hat{\lambda}_{33}$ will increase by the same factor, so things go wrong when $\hat{\lambda}_{33}$ is negative and the terrain is too steep. This typically happens near the ground where the transformation can result in too large speed up factors.

It should be noted that first order solutions do exist even if $1+\hat{\lambda}_{33}$ changes sign somewhere. A division by zero does not occur because $1/(1+\hat{\lambda}_{33}) \sim 1-\hat{\lambda}_{33}$ to first order. However, strange things do happen: the map may not be one–to–one and points in the air may be mapped to points in the ground. In any case the linear approximation is not justified unless $\hat{\lambda}_{33}$ is small compared to 1. It might be better to use the linearized Jacobian matrix which is the one that enters the linearized equations for λ, viz.

$$u = (1-\hat{\lambda}_{22}-\hat{\lambda}_{33})\,\acute{u} \tag{29}$$

$$v = \hat{\lambda}_{21}\,\acute{u} \tag{30}$$

$$w = \hat{\lambda}_{31}\,\acute{u} \tag{31}$$

This avoid excessive speed–up factors, but it is not necessarily very accurate because the perturbations are in any case too large to justify a linear approximation.

3 Results and Discussion

3.1 Axisymmetric Gaussian hill with a moderate slope ($\alpha = 17^\circ$)

In this section, the results of the Cases 1-8 are discussed, which represent an axisymmetric Gaussian hill with a moderate slope angle of 17°. Figure 5 depicts streamlines that originate at the bottom and top of the AD for Cases 1-8. Figure 6 depicts streamlines that originate at the left and right side of the AD for Cases 1-8. The circles in Figure 6 represent height contours with a radial interval of one standard deviation. Figures 5 and 6 show results of EllipSys3D RANS with and without AD, together with results from the terrain flow model of Fuga (where no AD is present). Both figures shows that the streamlines of the wind turbine wake in RANS are comparable with a RANS simulation without an AD, although height differences between the streamlines are visible especially for Cases 1 and 2 (Figure 5) For Case 1, the height difference between the streamlines at $x/H = -5$ and $x/H = 5$ for a RANS simulation with and without AD is about 0.1H and 0.2H, respectively. While for Case 2, the height difference between the streamlines at the hill top and $x/H = 5$ for a RANS simulation with and without AD is about 0.2H and 0.3H, respectively. This indicates that the wake in RANS follows the terrain streamlines up to a certain extend.

The streamlines of Fuga are comparable with the streamlines of RANS (without AD). For Cases 1, 3 and 7, the height difference at $x/H = \pm 5$ between the streamlines computed by RANS and Fuga are within 0.1H (as depicted in Figure 5). The difference is slightly larger for Case 5: 0.1H to 0.14H. For Cases 2, 4, 6 and 8, the height difference between the streamlines at the top of the hill $x/H = 0$ is well within 0.1H. The difference in horizontal distance between the streamlines is smaller for Cases 1-6: less than 0.05H (taken at the same locations as discussed previously and depicted in Figure 6). For Cases 7 and 8 the difference in horizontal distance between the streamlines is slightly larger: 0.05-0.1H.

Contours of the speed factor in a xz plane of Cases 1 and 3 (without AD) are depicted in Figure 7, where results of RANS and terrain flow model of Fuga are compared. Since only results without AD are considered, Cases 1 ($y = 0$) and 3 ($y = \sigma$) represent Cases 1-8. The overall speed up factor of Fuga compares well with RANS, while deviations are observed near the hill surface. Differences in the order of 0-20% are seen at the hill upstream of the top for Case 1 ($y = 0$), while large difference are found in the wake of the hill for both cases (70% $<$ for Case 1).

Speed up factor profiles at the AD location (without AD) for Cases 1 and 3 (which represent Cases 1-8) are shown in Figure 8 for RANS and the terrain flow model of Fuga. The speed profiles are very similar and only deviate less than 2% above $H/10$. The difference increase towards the surface. Hence, if a wind turbine is small compared to the hill height, the difference in speed profile may be significant.

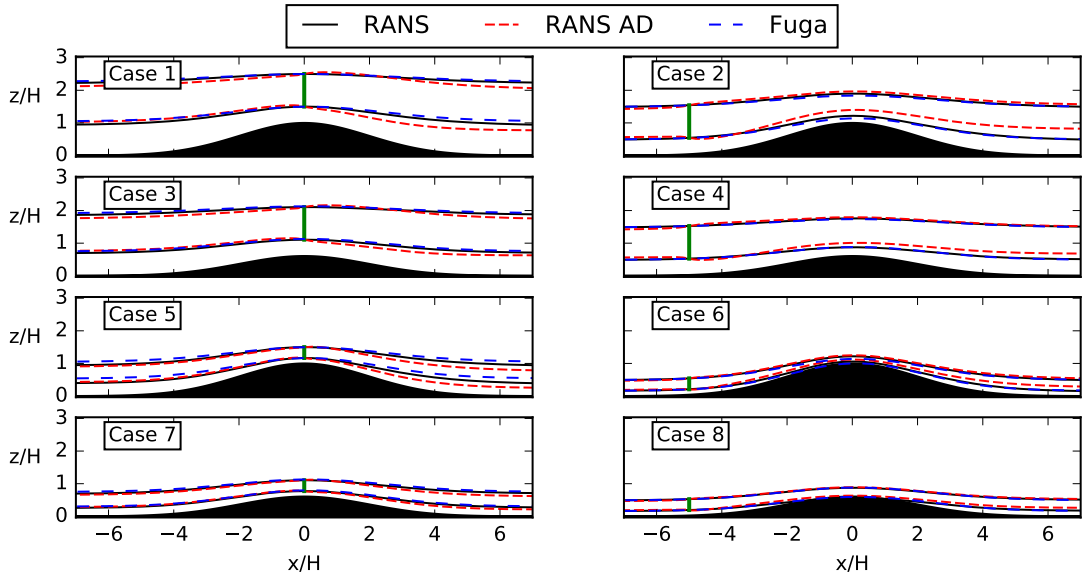

Figure 5: Side view comparison of streamlines from RANS and Fuga for Cases 1-8. Green line represents AD.

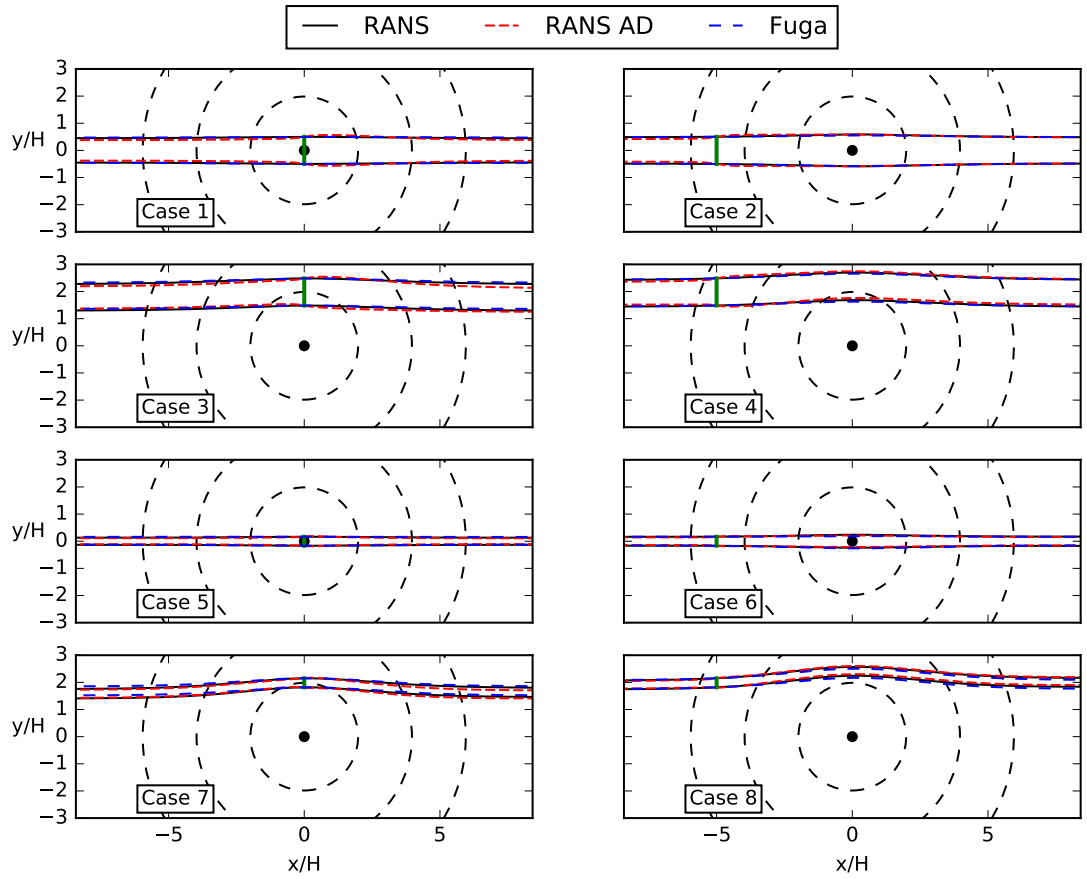

Figure 6: Top view comparison of streamlines from RANS and Fuga for Cases 1-8. Dashed circles are height contours with an interval of one standard deviation. Green line represents AD.

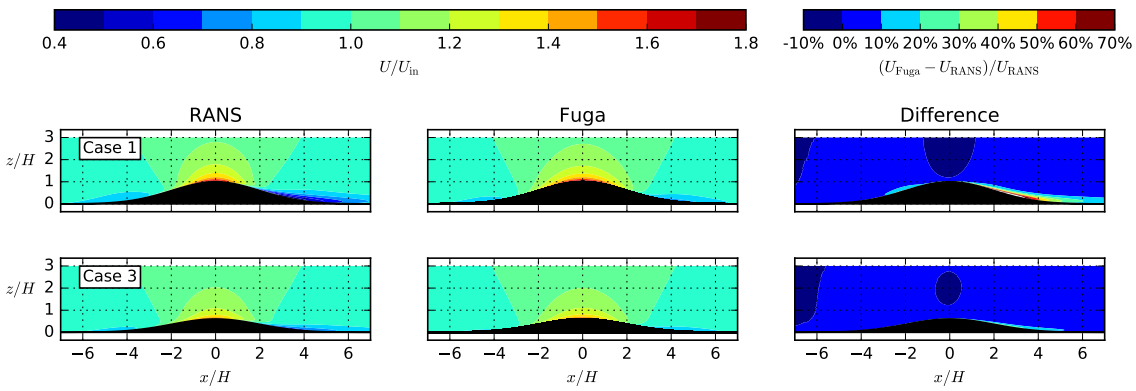

Figure 7: Speed up factor at $y = y_{AD}$ from RANS (without AD) and Fuga for Cases 1 and 3.

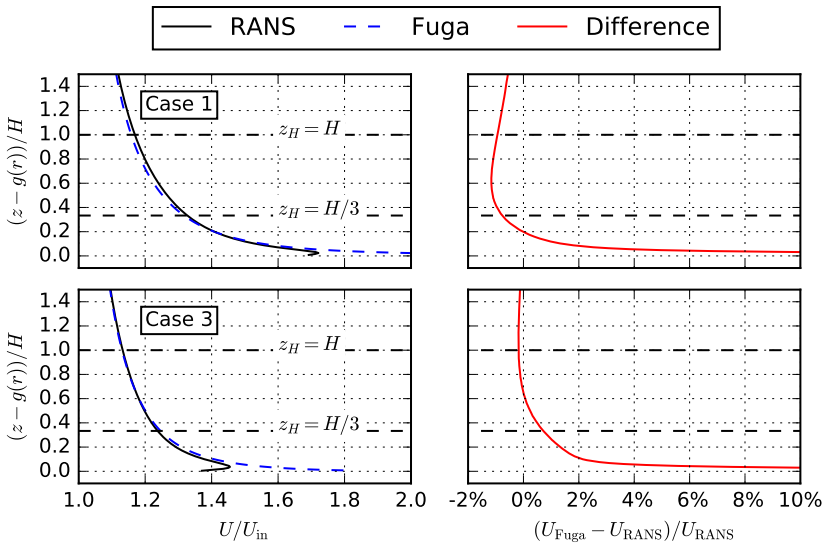

Figure 8: Speed up factor at $\{x, y\} = \{x_{AD}, y_{AD}\}$ from RANS (without AD) and Fuga as function of the distance above terrain for Cases 1 and 3. U_{in} represents inflow profile.

3.2 Axisymmetric Gaussian hill with high slopes

In this section, the results of the Cases 9-12 are discussed, which represent an axisymmetric Gaussian hill with an increasing slope angle of 20, 25, 30 and 40°.

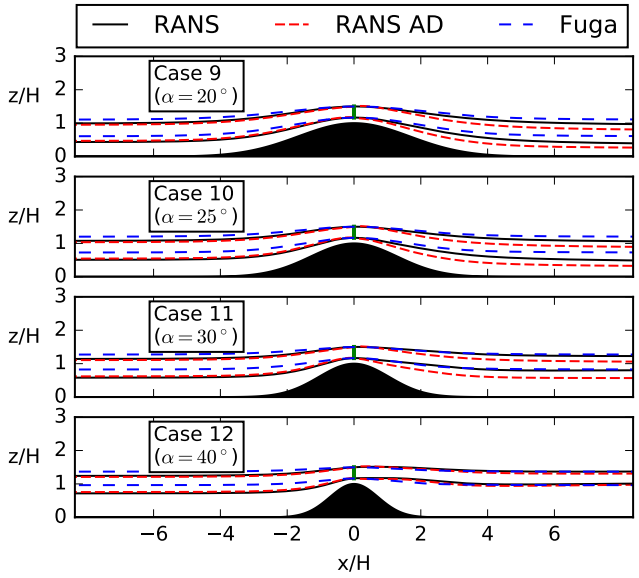

Figure 9: Side view comparison of streamlines from RANS and Fuga for Cases 9-12. Green line represents AD.

Streamlines that originate from the bottom and the top of the AD, are shown in Figure 9 for Cases 9-12. Two RANS results are shown that represent simulations with and without an AD. As seen previously in for the axisymmetric Gaussian hill for a moderate slope angle (Figures 5 and 6, the wake follows the terrain reasonably well, the largest differences at $x/H = 5$ are found for a slope angle of 30°: 0.22H. The best downstream comparison of the RANS streamlines in Figure 9 is found for the largest slope angle of 40° which is caused by the large recirculation region on the lee side of the hill. In other words, the recirculation region is a more dominant flow feature compared to the wind turbine wake. The streamlines of the terrain model of Fuga are also plotted in Figure 9, and are comparable with the RANS without an AD. For the three highest slope angles (30 and 40°), the largest differences between the models are observed upstream of the hill, which is a surprising result. The height difference of the streamlines at $x/H = -5$ between Fuga and RANS is 0.1H to 0.25H for all cases, where the largest difference (0.25H) is found for the highest slope angle (40°) at $x/H = -5$, while this difference is only 4% at $x/H = 5$ for the same slope angle. The largest height difference between the streamlines at $x/H = 5$ computed by RANS and the terrain model of Fuga is found for a slope angle of 25°: 0.2H.

Figure 10 depicts the speed up factor of Cases 9-12 computed by the RANS model and the terrain flow model of Fuga. The RANS model predicts flow separation and a recirculations zone behind the hill slope beyond a slope angle of 25°. Since the terrain flow model in Fuga is linear, it cannot predict these flow features. As a result, the difference between RANS and Fuga is large (above 100%) in the wake of the hill. However, the difference in speed up factor at the top of the hill between RANS and Fuga are small, also for large hill angles.

Figure 11 shows the speed up factor profile at the hill top for Cases 9-12 calculated with RANS (without AD) and the terrain flow model of Fuga. The largest difference between the models is about 4% above $H/10$ for Case 10, which is larger than found for moderate slope angles (Figure 8), but much smaller than one would expect. Surprisingly, the difference in speed up factor is smaller for Case 12, which has the largest hill angle. A possible reason could be than if the hill angle is large, the separation region behind the hill in RANS is making the effective hill curvature at the top less since a part of the wind flows straight over the recirculation zone.

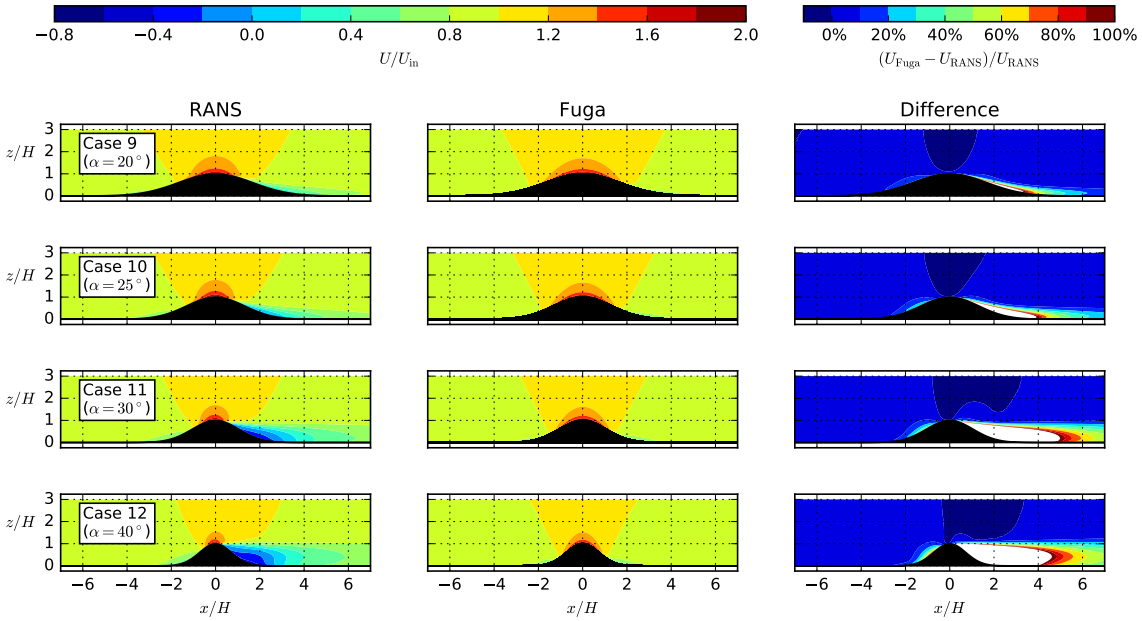

Figure 10: Speed up factor at $y = y_{AD}$ from RANS (without AD) and Fuga for Cases 9-12. White area in right plots are differences above 100%.

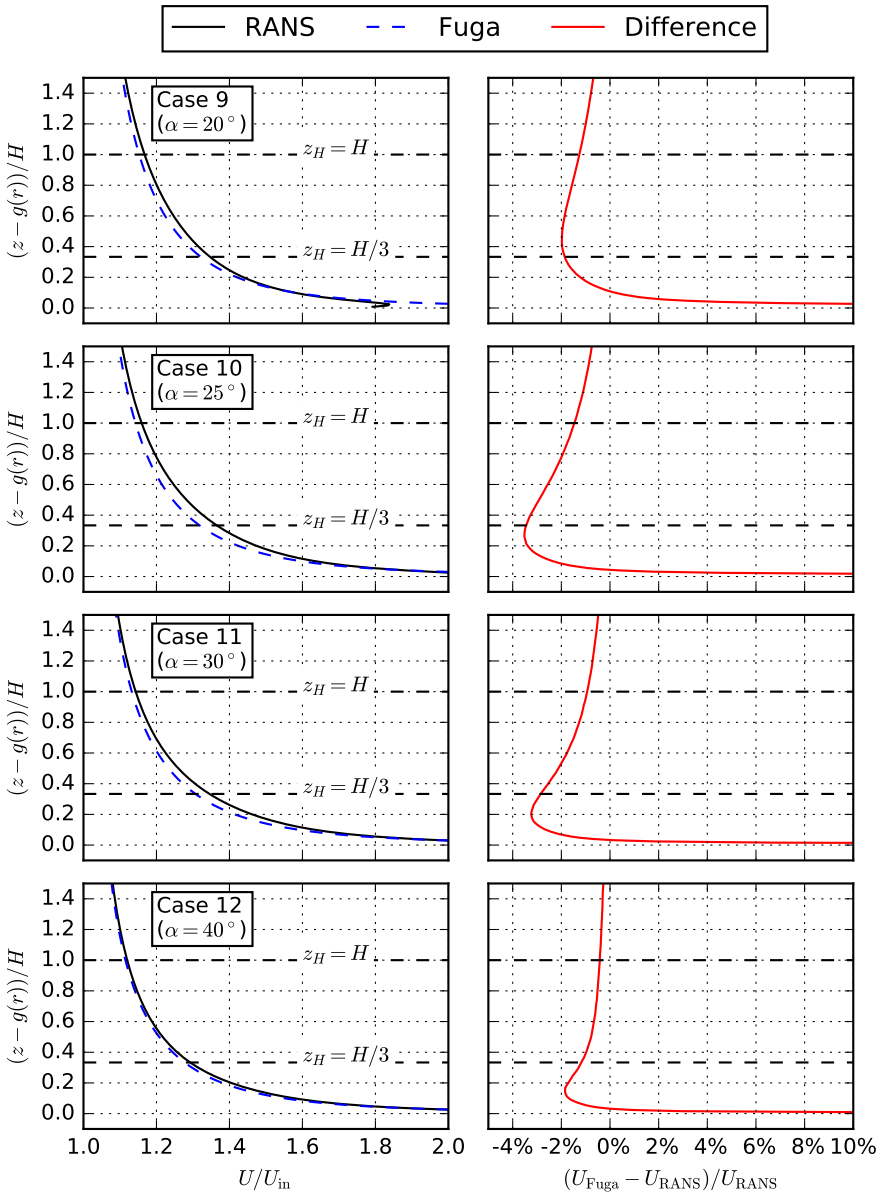

Figure 11: Speed up factor at $x, y = x_{AD}, y_{AD}$ from RANS (without AD) and Fuga as function of the distance above terrain for Cases 9-12. U_{in} represents inflow profile. Right column shows the difference between RANS and Fuga in horizontal velocity.

3.3 Shaanxi complex terrain site

In this section, the results of the Cases 13-15 are discussed, which represent the Shaanxi complex terrain site with three different scaling factors: 0.1, 0.5 and 1.

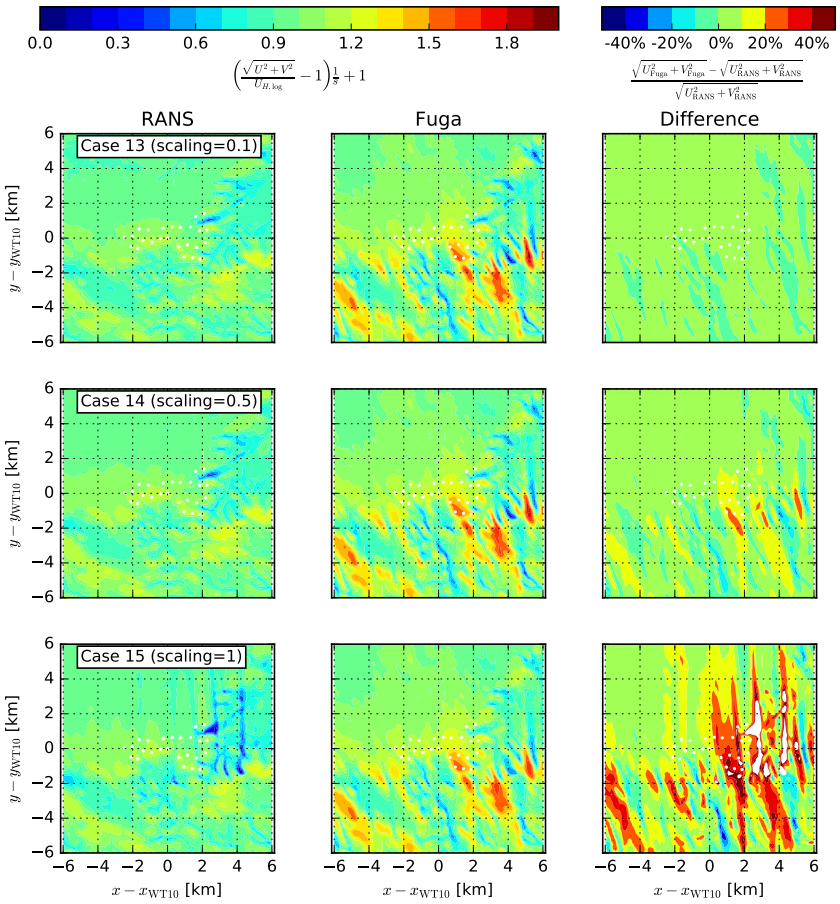

Figure 12: (Scaled) speed up factor at z_H above terrain predicted by RANS (without ADs and employing the k-ε-f_P turbulence model) and Fuga for Cases 13-15 (representing three different terrain height scaling factors).

Figure 12 depicts the speed up factor, normalized by the scaling factor such that speed up factor of the Cases 13, 14 and 15 can be compared with each other. Results of RANS and the terrain model of Fuga are shown, together with the relative difference in terms of horizontal velocity. The RANS model predicts similar scaled speed up factors for a scaling of 0.1 and 0.5 but a different speed up factor flow pattern is observed for a scaling of 1, where large areas of flow separation are present. The scaled speed up factors calculated by Fuga are very similar across all cases. When comparing RANS with Fuga, it is clear that large differences in the scaled speed up factor occur South and East of the wind farm where the largest slope angles are present as depicted in Figure 2. As expected, the differences between RANS and Fuga in terms of horizontal velocity increase with larger scaling factors. This is shown by the most right plots of Figure 12, especially for the east part of the wind farm where the RANS model predicts large areas of flow separation for a scaling of 1.

Figures 13, 14 and 15 show the horizontal velocity profiles at the twenty five wind turbine locations for Cases 13-15. Results of RANS simulations are compared with the terrain model of Fuga and logarithmic inflow profile. For each case, two RANS simulations results are depicted that show the difference bewteen the standard k-ε turbulence model and k-ε-f_P turbulence model. For a scaling factor of 0.1 and 0.5, both turbulence models predict very similar velocity profiles, as shown by Figures 13 and 14. However, for a

scaling factor of 1 (see Figure 14), the turbulence models predict different velocity profiles for WTs 19, 20 and 21. These wind turbines are located close to regions where the flow is recirculating. In these areas, the velocity gradients are high and the k-ε-f_P model delays the turbulent mixing compared to the standard k-ε model which affects the velocity profiles at WTs 19, 20 and 21. The comparison of the RANS turbulence models shows that the influence of the turbulence model is significant when the terrain is very complex.

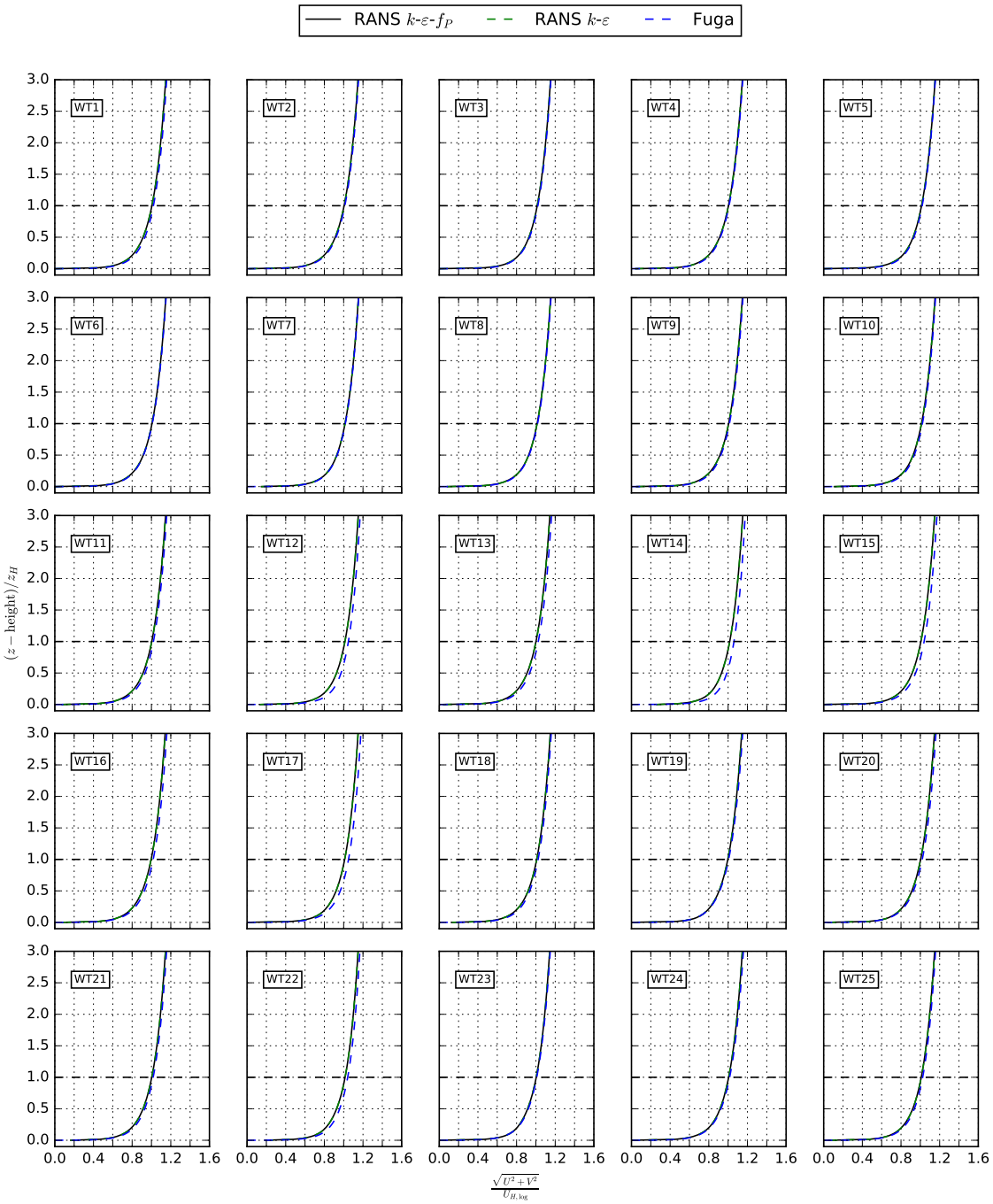

Figure 13: Speed up factor profiles at $\{x, y\} = \{x_{AD}, y_{AD}\}$ from RANS (without ADs) and Fuga for Case 13 (scaling of 0.1). Two results of RANS are shown using different turbulence models

For a scaling factor of 0.1 and 0.5, the differences in velocity profiles from RANS and Fuga are small. However, for a scaling factor of 1, the difference in velocity profile between RANS and Fuga becomes large, especially when moving towards the ground, as shown in Figure 15. The profiles at WT 12 and 14

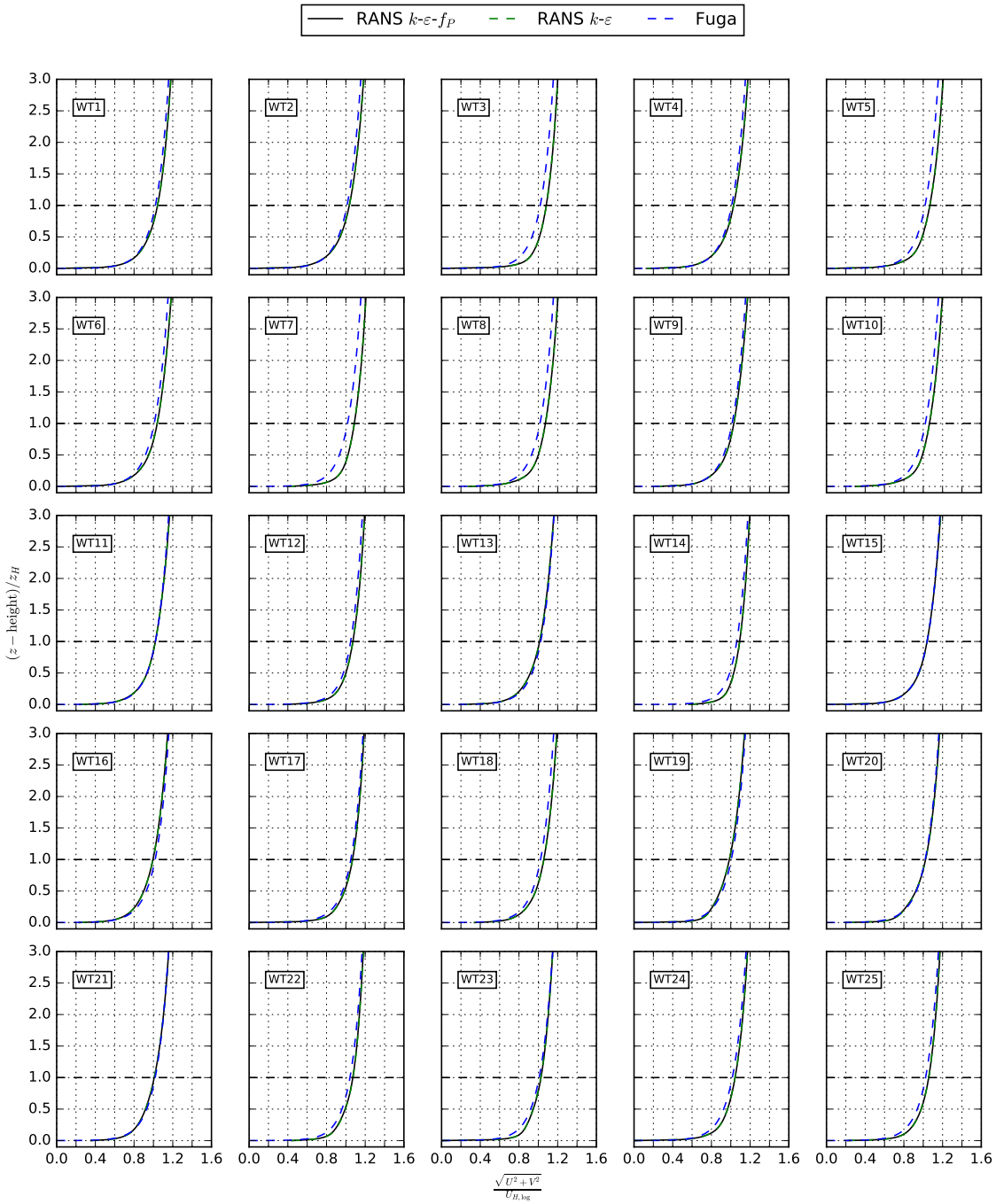

Figure 14: Speed up factor profiles at $\{x,y\} = \{x_{AD}, y_{AD}\}$ from RANS (without ADs) and Fuga for Case 14 (scaling of 0.5). Two results of RANS are shown using different turbulence models

show nonphysically large speed up factors near ground. These wind turbines are located downstream of an area where large terrain slope angles are presented as depicted in Figure 2. This shows that the terrain model of Fuga is not capable of calculating the velocity profiles at the wind turbine locations for a scaling factor of 1.

The horizontal velocity at hub height of the twenty five wind turbines are listed in Table 3 for RANS and Fuga using Cases 13-15. The largest relative difference between the models are 4.3%, -6.4% and 43% for the terrain scaling factor of 0.1, 0.5 and 1. Hence, Fuga performs well for Cases 13 and 14 but cannot

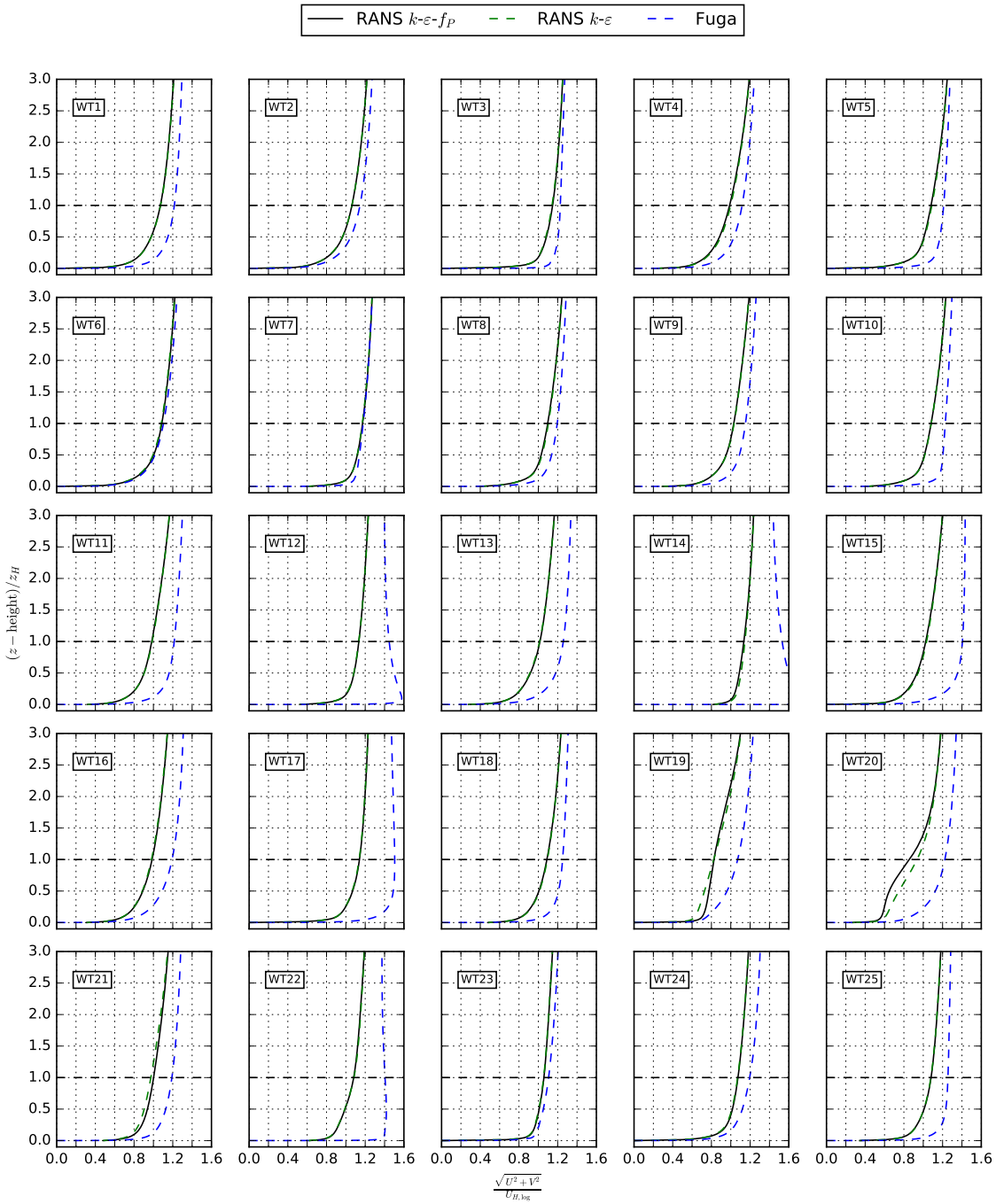

Figure 15: Speed up factor profiles at $\{x, y\} = \{x_{AD}, y_{AD}\}$ from RANS (without ADs) and Fuga for Case 15 (scaling of 1). Two results of RANS are shown using different turbulence models

capture the speed up factor for Case 15 where the terrain is too complex for a linear terrain flow model.

Table 3: Speed up factor ($\sqrt{U^2+V^2}/U_{H,\log}$) at $\{x,y\} = \{x_{AD}, y_{AD}\}$ from RANS (without ADs and employing the k-ε-f_P turbulence model) and Fuga for Cases 13-15 (representing three different terrain height scaling factors). The largest error per case are presented in bold numbers.

	Case 13 (scaling=0.1)			Case 14 (scaling=0.5)			Case 15 (scaling=1)		
WT	RANS	Fuga	Difference	RANS	Fuga	Difference	RANS	Fuga	Difference
1	1.00	1.02	1.54%	1.04	1.02	-2.13%	1.07	1.22	13.44%
2	1.00	1.01	0.75%	1.04	1.01	-2.25%	1.06	1.15	7.82%
3	1.01	1.02	0.63%	1.08	1.02	-5.75%	1.15	1.23	6.91%
4	1.00	1.01	0.59%	1.03	1.01	-1.97%	0.99	1.12	13.08%
5	1.01	1.02	0.63%	1.07	1.02	-4.60%	1.08	1.21	12.01%
6	1.01	1.01	0.24%	1.04	1.01	-3.01%	1.09	1.10	1.58%
7	1.01	1.02	0.30%	1.09	1.02	**-6.47%**	1.17	1.18	0.52%
8	1.01	1.02	0.44%	1.07	1.02	-5.20%	1.10	1.20	8.97%
9	1.01	1.01	0.83%	1.03	1.01	-1.72%	1.03	1.15	11.71%
10	1.01	1.02	0.95%	1.06	1.02	-4.01%	1.08	1.23	13.53%
11	1.00	1.02	1.73%	1.02	1.02	0.02%	0.98	1.22	23.62%
12	1.01	1.05	3.54%	1.07	1.05	-2.17%	1.13	1.45	27.62%
13	1.00	1.02	2.35%	1.01	1.02	1.11%	1.02	1.26	23.72%
14	1.02	1.06	**4.32%**	1.09	1.06	-2.77%	1.14	1.53	34.85%
15	1.01	1.04	3.30%	1.04	1.04	0.02%	1.03	1.41	36.96%
16	1.00	1.02	2.12%	1.00	1.02	2.28%	0.99	1.19	20.92%
17	1.01	1.05	3.92%	1.07	1.05	-1.65%	1.14	1.50	31.95%
18	1.01	1.02	1.42%	1.06	1.02	-3.18%	1.09	1.25	14.88%
19	1.00	1.01	0.85%	0.99	1.01	2.00%	0.83	1.07	29.76%
20	1.00	1.02	1.68%	1.02	1.02	-0.37%	0.86	1.22	**42.80%**
21	1.00	1.02	1.46%	1.01	1.02	0.92%	1.00	1.19	18.87%
22	1.01	1.04	2.66%	1.07	1.04	-2.78%	1.08	1.40	29.96%
23	1.00	1.01	0.53%	1.03	1.01	-1.85%	1.06	1.11	4.57%
24	1.01	1.02	1.02%	1.04	1.02	-2.75%	1.07	1.20	11.26%
25	1.01	1.02	1.44%	1.06	1.02	-3.05%	1.08	1.26	16.14%

4 Conclusion

A recently developed linearized terrain flow model of Fuga is compared with non linear RANS simulations of flow over terrain using fiveteen test cases. Twelve test cases are based on an axisymmetric Gaussian hill with and without a single wind turbine, using four different wind turbine locations, two rotor diameters and five different slope angles. Three test cases are based on a real onshore wind farm located in a mountainous area in the Shaanxi province of China, where the terrain height is scaled by a factor 0.1, 0.5 and 1.

The RANS simulations of the axisymmetric Gaussian hill show that flow separation starts to occur for a slope angle of 30°, where a large recirculation zone is visible on the lee side of the hill. In addition, the RANS simulations of the axisymmetric Gaussian hill with and without wind turbine show that the streamlines of the wake follow the streamlines of the terrain, but height differences between a streamline with and without wind turbine can be as large as 30% of the hill height. For highest slope angle of 40°, these difference are the largest upstream, while the downstream streamlines with and without wind turbine match very well. This is a surprising result but it could be explained by the fact that the re-circulation zone of the hill is a more dominant flow phenomenon compared to the wind turbine wake. The streamlines of the terrain model of Fuga are also compared with the streamlines of RANS (without AD) for the axisymmetric Gaussian hill test cases. For a moderate slope angle of 17°, the height difference between streamlines is found to be less than 15% of the hill height, while a larger difference of 25% of the hill height is found for a slope of angle of 40°(observed upstream of the hill).

The terrain model of Fuga cannot predict flow separation due to the linear nature of the model, hence, it cannot predict the speed up factor in the wake of the hill for slope angles beyond 25°. For smaller slope angles, the error in the wake of the hill decreases and is mainly occurring near the ground. The speed up factor on top of the hill from the terrain model of Fuga compares very well with RANS even for the highest slope angle of 40°. This indicates the wind resources for a wind turbine on top of a hill can be predicted by Fuga with a similar accuracy as RANS, as long as such a wind turbine does no operate in the wake of upstream hills.

The test cases based on the Shaanxi complex terrain show that different turbulence models in RANS predict different velocity profiles if the flow solution includes recirculation zones. In addition, Fuga cannot predict the speed up factors at the Shaanxi wind farm at the wind turbine locations where the terrain slopes are too high and flow separation occurs in the RANS simulations. For these wind turbine locations, Fuga also has problems near the wall. When the terrain height is scaled down to 50%, the terrain model of Fuga compares well with RANS in terms of speed up factor (largest difference less than 7% at hub height) and velocity profiles at the wind turbine locations.

References

[1] A. Bechmann, N. N. Sørensen, J. Berg, J. Mann, and P.-E. Réthoré, "The Bolund Experiment, Part II: Blind Comparison of Microscale Flow Models," Boundary-Layer Meteorology, 2011. [Online]. Available: https://link.springer.com/article/10.1007%2Fs10546-011-9637-x

[2] T. Göçmen, M. P. van der Laan, P. E. Réthoré, A. Peña Diaz, G. C. Larsen, and S. Ott, "Wind turbine wake models developed at the technical university of Denmark: A review," Renewable and Sustainable Energy Reviews, vol. 60, pp. 752–769, 2016. [Online]. Available: https://www.sciencedirect.com/science/article/pii/S136403211600143X

[3] S. Ott, J. Berg, and M. Nielsen, "Linearised CFD Models for Wakes," Risø, Tech. Rep. Risø-R-1772, 2011. [Online]. Available: http://orbit.dtu.dk/files/6354851/ris-r-1772.pdf

[4] A. S. Monin and A. M. Obukhov, "Basic laws of turbulent mixing in the surface layer of the atmosphere," Tr. Akad. Nauk. SSSR Geofiz. Inst., vol. 24, pp. 163–187, 1954 (translated by John Miller, 1959).

[5] N. N. Sørensen, "General purpose flow solver applied to flow over hills," Ph.D. dissertation, Risø National Laboratory, Roskilde, Denmark, 1994. [Online]. Available: http://orbit.dtu.dk/files/12280331/Ris_R_827.pdf

[6] J. A. Michelsen, "Basis3d - a platform for development of multiblock PDE solvers." Technical University of Denmark, Lyngby, Denmark, Tech. Rep. AFM 92-05, 1992.

[7] M. Sessarego, W. Z. Shen, M. P. van der Laan, K. S. Hansen, and W. J. Zhu, "CFD simulations of a wind farm in complex terrain and comparisons to measurements." Applied Sciences, vol. 8, no. 5, 2018. [Online]. Available: http://www.mdpi.com/2076-3417/8/5/788

[8] USGS, "Shuttle radar topography mission (srtm)," U.S. Geological Survey, Tech. Rep., 2009. [Online]. Available: https://pubs.usgs.gov/fs/2009/3087/

[9] M. P. van der Laan, N. N. Sørensen, P.-E. Réthoré, J. Mann, M. C. Kelly, N. Troldborg, J. G. Schepers, and E. Machefaux, "An improved k-ε model applied to a wind turbine wake in atmospheric turbulence," Wind Energy, vol. 18, no. 5, pp. 889–907, May 2015. [Online]. Available: https://onlinelibrary.wiley.com/doi/abs/10.1002/we.1736

[10] P. A. Taylor and H. W. Teunissen, "The askervein hill project: Overview and background data," Boundary-Layer Meteorol, vol. 39, no. 15, pp. 15–39, 1987. [Online]. Available: https://doi.org/10.1007/BF00121863

[11] R. Mikkelsen, "Actuator Disc Methods Applied to Wind Turbines," Ph.D. dissertation, Technical University of Denmark, Mek dept, Lyngby, Denmark, 2003.

[12] N. N. Sørensen, A. Bechmann, J. Johansen, L. Myllerup, P. Botha, S. Vinther, and B. S. Nielsen, "Identification of severe wind conditions using a Reynolds Averaged Navier-Stokes solver," Journal of Physics: Conference series, vol. 75, no. 012053, pp. 1–13, 2007. [Online]. Available: http://iopscience.iop.org/article/10.1088/1742-6596/75/1/012053

A Grid sensitivity study of the horizontal spacing in RANS simulations of the Shaanxi complex terrain site

The influence of the horizontal spacing inside the 10×10 km^2 area of the grid (Figure 4) is shown in Figure 16 for RANS three simulations of the Shaanxi complex terrain site with a scaling factor of 1 (Case 15). The k-ε-f_P turbulence model is employed and a horizontal grid spacing of 20, 40 and 80 m is simulated. (The simulation in this report are performed with a 40 m grid spacing.) The input surface map of the terrain has a horizontal spacing of 40 m and is kept constant within the three RANS simulations. Figure 16 depicts

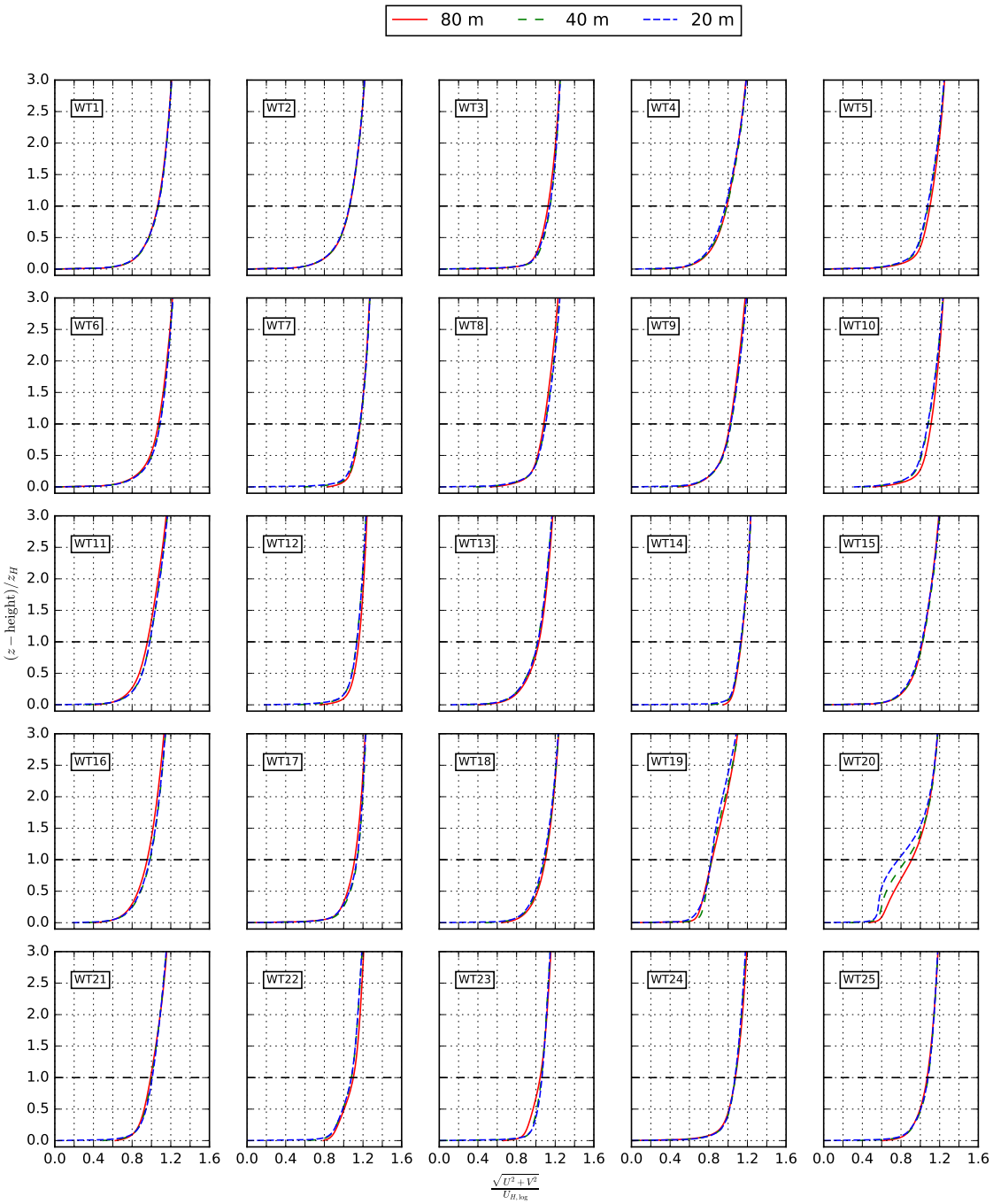

Figure 16: Grid sensitivity study of speed up factor profiles at $\{x,y\} = \{x_{AD}, y_{AD}\}$ from RANS (without ADs and employing the k-ε-f_P turbulence model) for Case 15 (scaling of 1).

velocity profiles at all twenty-five wind turbine locations for all three grid sizes. Results of 20 and 40 m grid spacings are very similar for most wind turbine locations; however, at WTs 19 and 20 the velocity profile between 20 and 40 m grid spacings are different. At these locations, recirculation zones are present and a grid refinement beyond 20 m is necessary.

DTU Wind Energy
Department of Wind Energy
Technical University of Denmark

Risø Campus Building 118
Frederiksborgvej 399
DK-4000 Roskilde
www.vindenergi.dtu.dk

DTU Wind Energy E-0173
ISBN: 978-87-93549-41-8